Supplement of Atmos. Chem. Phys., 22, 11739–11757, 2022
https://doi.org/10.5194/acp-22-11739-2022-supplement

Atmospheric Chemistry and Physics
Open Access

Supplement of

The impact of atmospheric motions on source-specific black carbon and the induced direct radiative effects over a river-valley region

Huikun Liu et al.

Correspondence to: Qiyuan Wang (wangqy@ieecas.cn) and Junji Cao (jjcao@mail.iap.ac.cn)

Text S1. Minimum R-squared method

The minimum R squared method developed by Wu et al., (2016) was used to separate secondary organic carbon (SOC) from the primary organic carbon (POC). The assumption behind this method is the organic carbon (OC) from non-combustion source is negligible. As explained by Wang et al., (2019), the major non-combustion source is biogenic which is mainly exists in coarse mode. Thus, the non-combustion organic carbon is considered negligible in this study. Therefore, SOC and POC can be separated by using following equations. For each date set, the ratios of OC to eBC and SOC and the R^2 between eBC and SOC can be calculated. SOC and eBC are considered independent, so the (OC/eBC)pri should be the value obtained when the R^2 between eBC and SOC is minimum.

$$\mathrm{POC} = (\mathrm{OC/EC})_{\mathrm{pri}} \times \mathrm{EC} \quad \text{(S1)}$$

$$\mathrm{SOC} = \mathrm{OC}_{\mathrm{total}} - (\mathrm{OC/EC})_{\mathrm{pri}} \times \mathrm{EC} \quad \text{(S2)}$$

where EC in this study is eBC. The $(OC/EC)_{pri}$ is the ratio in freshly emitted OC and EC from combustion sources.

The light absorption at shorter wavelengths (<660nm) is not only from primary light absorbing substances but also from the secondary organic carbon (Wang et al., 2019). The assumption for this method is that the light absorption caused by non-combustion sources is negligible. As mentioned above, most of the biogenic BrC is in coarse mode. Another common light absorbing substance is the Fe_2O_3 in the dust, but the impact of that should be limited because the absorption from Fe_2O_3 in the dust has been reported to be much smaller than that from BC (Ramachandran and Kedia, 2010). Thus, to separate the secondary light absorption ($b_{abs}(\lambda)_{secondary}$) from the primary light absorption ($b_{abs}(\lambda)_{primary}$), a BC-tracer method coupled with a minimum R-squared method was used. The equations used for the calculation are follows:

$$b_{\mathrm{abs}}(\lambda)_{\mathrm{secondary}} = b_{\mathrm{abs}}(\lambda) - \left(\frac{b_{\mathrm{abs}}(\lambda)}{\mathrm{BC}}\right)_{\mathrm{pri}} \times \mathrm{BC} \quad \text{(S3)}$$

$$b_{\mathrm{abs}}(\lambda)_{\mathrm{primary}} = b_{\mathrm{abs}}(\lambda) - b_{\mathrm{abs}}(\lambda)_{\mathrm{secondary}} \quad \text{(S4)}$$

Where $b_{\mathrm{abs}}(\lambda)$ is the light absorption at different wavelengths (λ=370nm, 470nm, 520nm, 590nm, 660nm) measured by AE33, BC is the eBC measured by AE33 at a wavelength of 880nm. The $\left(\frac{b_{\mathrm{abs}}(\lambda)}{\mathrm{BC}}\right)_{\mathrm{pri}}$ is the ratio of the primary light absorption to the BC mass concentration from combustion sources.

Reference:

Ramachandran, S., and Kedia, S., Black carbon aerosols over an urban region: radiative forcing and climate impact, Journal of Geophysical Research, 115, D10202, doi:10.1029/2009JD013560, 2010.

Wang, Q., Han, Y., Ye, J., Liu, S., Pongpiachan, S., Zhang, N., Han, Y., Tian, J., Wu, C., Long, X., Zhang, Q., Zhang, W., Zhao, Z., and Cao, J.: High contribution of secondary brown carbon to aerosol light absorption in the southeastern margin of Tibetan Plateau, Geophys. Res. Lett., 46, 4962–4970, https://doi.org/10.1029/2019GL082731, 2019

Wu, C., & Yu, J. Z. (2016). Determination of primary combustion source organic carbon-to-elemental carbon (OC/EC) ratio using ambient OC and EC measurements: Secondary OC-EC correlation minimization method. Atmospheric Chemistry and Physics, 16(8), 5453–5465. https://doi.org/10.5194/acp-16-5453-2016

Text S2. Cluster analysis of air-mass trajectories

Back trajectories were calculated by using Hybrid Single-Particle Lagrangian Integrated Trajectory (HYSPLIT) model (Draxler and Hess, 1998) developed by the Air Resource Lab (ARL) of the National Oceanic and Atmospheric Administration (NOAA). The model can predict the position of air mass by using mean wind. The back-in-time positions are calculated by reversing the advection equation (Draxler and Hess, 1997). The calculation requires the mean wind, for calculating trajectories, only advection is considered (Stein et al., 2015). The basic equations for trajectory calculation in HYSPLIT are as follows:

$$P'(t+\Delta t) = P(t) + V(P,t) \times \Delta t \quad \text{(S5)}$$

$$P(t+\Delta t) = P(t) + 0.5 \times [V(P,t) + V\left(P', t+\Delta t\right)] \times \Delta t \quad \text{(S6)}$$

Where $P(t)$ is the initial position, $P'(t+\Delta t)$ is the first guess position, V is the average velocity, t is the time, Δt is the time step.

A large number of 24 h trajectories (793) that were retrieved for the study period showed diverse pathways, so in order to find out the representative pathways for those trajectories, a cluster analysis based on an angle-based distance statistics method was conducted. Compared with Euclidean distance, angle-based distance statistics method focuses on the direction of air mass instead of the speed. The angle-based distance statistics method is defined by following equations (Sirois and Bottenheim, 1995):

$$d_{12} = \frac{1}{2}\sum_{i=1}^{n} cos^{-1}(0.5 \times \frac{A_i + B_i - C_i}{\sqrt{A_i B_i}}) \quad \text{(S7)}$$

$$A_i = (X_1(i) - X_0)^2 + (Y_1(i) - Y_0)^2 \quad \text{(S8)}$$

$$B_i = (X_2(i) - X_0)^2 + (Y_2(i) - Y_0)^2 \quad \text{(S9)}$$

$$C_i = (X_2(i) - X_1(i))^2 + (Y_2(i) - Y_1(i))^2 \quad \text{(S10)}$$

Where d_{12} is the average angle between the two backward trajectories, varying between 0 and π; X_0 and Y_0 are the position of the receptor site; and X_1 (Y_1) and X_2 (Y_2) are the backward trajectories 1 and 2, respectively. In this study, three clusters were chosen as representative of the backward trajectory clusters based on the total spatial variance (TSV) value. The simulation was conducted using the GIS-based TrajStat software (Wang et al., 2009).

Reference

Sirois, A. and Bottenheim, J. W.: Use of backward trajectories to interpret the 5-year record of PAN and O3 ambient air concentrations at Kejimkujik National Park, Nova Scotia, J. Geophys. Res., 100, 2867–2881, https://doi.org/10.1029/94JD02951, 1995.

Wang, Y. Q., Zhang, X. Y., and Draxler, R. R.: TrajStat: GISbased software that uses various trajectory statistical analysis methods to identify potential sources from long-term air pollution measurement data, Environ. Model. Softw., 24, 938–939, https://doi.org/10.1016/j.envsoft.2009.01.004, 2009.

Stein, A., Draxler, R., Rolph, G., Stunder, B., Cohen, M., and Ngan, F.: NOAA'S HYSPLIT atmospheric transport and dispersion modeling system, Bull. Amer. Meteor. Soc., 96, 2059-2077, https://doi.org/10.1175/BAMS-D-14-00110.1, 2015.

Draxler, R., and Hess, G.: An overview of the HYSPLIT_4 modelling system for trajectories, Aust. Meteorol. Mag., 47, 1998.

Draxler, R., and Hess, G.: Description of the Hysplit_4 Modeling System, NOAA technical memorandum ERL ARL-224, 1997.

Table S1. The seasonal meteorological data of Baoji

Season	Temperature (℃)	Relative humidity (%)	Precipitation in last hour (mm)
Winter	2.7	60.6	0.025
Spring	11.5	54.9	0.042
Summer	23.7	67.1	0.139
Autumn	20.2	67.0	0.074

Table S2. Data and parameters used in HYSPLIT model

Items	Data/parameters
Model	HYSPLIT
Meteorological data	GDAS data, 1° × 1°, 23 vertical levels, 3 hourly
Backward period	24h
Footprint level	100 m above the ground
Receptor site location	34°21′16.8″N, 107°12′59.6″E

Table S3. The results of Bootstrap (BS) and displacement (DISP)

DISP Diagnostics:					
	Error Code:	0			
	%dQ:	-1.772433856			
	Swaps by Factor:	0	0	0	0
BS Mapping:					
	Base Factor 1	Base Factor 2	Base Factor 3	Base Factor 4	Unmapped
Boot Factor 1	49	0	0	1	0
Boot Factor 2	0	50	0	0	0
Boot Factor 3	0	0	50	0	0
Boot Factor 4	2	0	0	48	0

Table S4. Mass absorption cross sections (MAC) and absorption Ångström exponents (AAE) derived from the positive matrix factorization model

	Diesel vehicular emissions	Coal combustion	Biomass burning	Fossil fuel combustion
MAC (m^2 g^{-1})	6.7	7.5	9.5	7.1
AAE	1.07	1.74	2.13	1.26

Table S5. Mean (range) BC mass concentration in river valley sites worldwide

Reference	BC concentration ($\mu g\ m^{-3}$)	Season	Topographic conditions	Altitude	Station type	Year
This study	3.63±2.73 (0.39~12.73)	November~December (winter)	river valley	450 to 800 m a.s.l.[a]	urban	2018
Glojek et al., (2020)	0.9~40	December~January (winter)	river valley	715 m a.s.l.	rural	2017-2018
Zhao et al. (2015)	25±11	January (winter)	river valley	410 m a.s.l.	urban	2013
Barman and Gokhale (2019)	20.58~22.44	Winter	river valley		urban	2016-2017
Zhang et al., 2020	0.102~1.525	Winter	river valley	2130 m a.s.l.	rural	2016-2017
Chakrabarty et al., (2012)	9~41	January~February (winter)	river valley		urban	2011
Zhao et al. (2019)	5.1 ± 2.1	December~January (winter)	river valley		urban	2018
Tiwari et al., 2016	8.19 ±1.39	December-February (winter)	river valley	55 m a.s.l.	urban	2013-2014

[a]asl stands for "above sea level."

References:

Barman, N., and Gokhale, S., Urban black carbon - source apportionment, emissions and long-range transport over the Brahmaputra River Valley, Sci. Total Environ., 693, 133577, https://doi.org/10.1016/j.scitotenv.2019.07.383, 2019

Chakrabarty, R., Garro, M., Wilcox, E., and Moosmuller, H., Strong radiative heating due to wintertime black carbon aerosols in the Brahmaputra River Valley, Geophys. Res. Lett., 39, L09804, https://doi.org/10.1029/2012GL051148, 2012.

Glojek, K., Moˇcnik, G., Alas, H., et al., The impact of temperature inversions on black carbon and particle mass concentrations in a mountainous area, Atmos. Chem. Phys., 22, 5577–5601, https://doi.org/10.5194/acp-22-5577-2022, 2022.

Zhang, X., Li, Z., Ming, J., and Wang, F., One-year measurements of equivalent black carbon, optical properties, and sources in the Urumqi River Valley, Tien Shan, China, Atmosphere, 11, 478, https://doi.org/10.3390/atmos11050478, 2020.

Zhao, S., Yu, Y., Yin, D., et al., Concentrations, optical and radiative properties of carbonaceous aerosols over urban Lanzhou, a typical valley city: results from in-situ observations and numerical model, Atmos. Environ., 213, 470–484, https://doi.org/10.1016/j.atmosenv.2019.06.046, 2019.

Zhao, S., Tie, X., Cao, J & Zhang, Q. (2015), Impacts of mountains on black carbon aerosol under different synoptic meteorology conditions in the Guanzhong region, China. Atmos. Res., 164-165, 286-296. http://dx.doi.org/10.1016/j.atmosres.2015.05.016

Tiwari, S., Kumar, R., Tunved, P., Singh, S., and Panicker, A., Significant cooling effect on the surface due to soot particles over Brahmaputra River Valley region, India: An impact on regional climate, 2016, Sci. Total Environ., 562, 504–516, http://dx.doi.org/10.1016/j.scitotenv.2016.03.157, 2016.

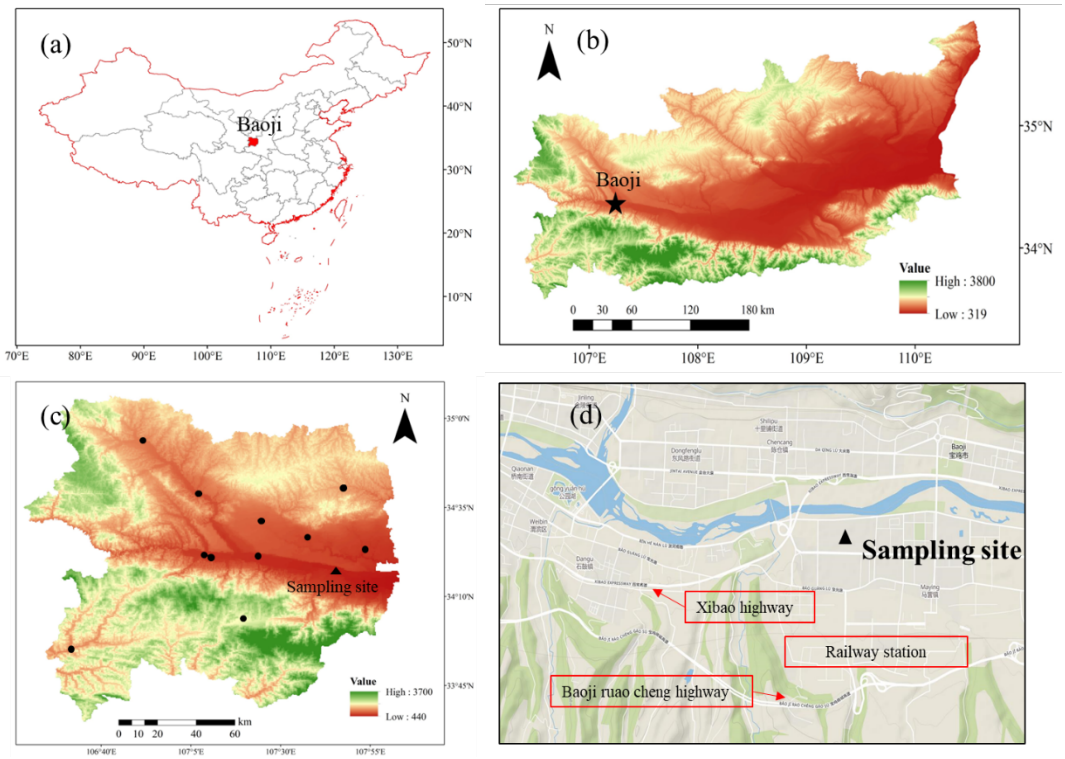

Figure S1. A map of the research site; (a) map of China—the red shape is the location of Baoji, (b) a map of the Guanzhong Plain, the black star represents the location of Baoji; (c) a map of Baoji City, the black dots and the black triangle represent 12 stations and the triangle is the location of sampling site, (d) a map of the sampling site from © Google (https://www.google.com /maps).

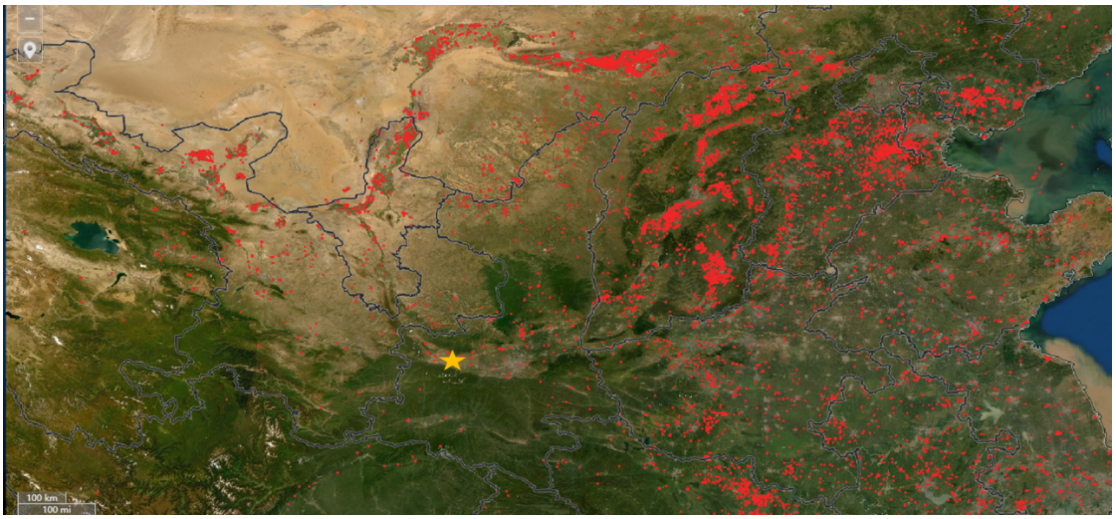

Figure S2. Map of fire occurrences. The yellow star represents the study site, the red dots represent the fire. The image from © NASA (National Aeronautics and Space Administration) (https://firms.modaps.eosdis.nasa.gov/map)

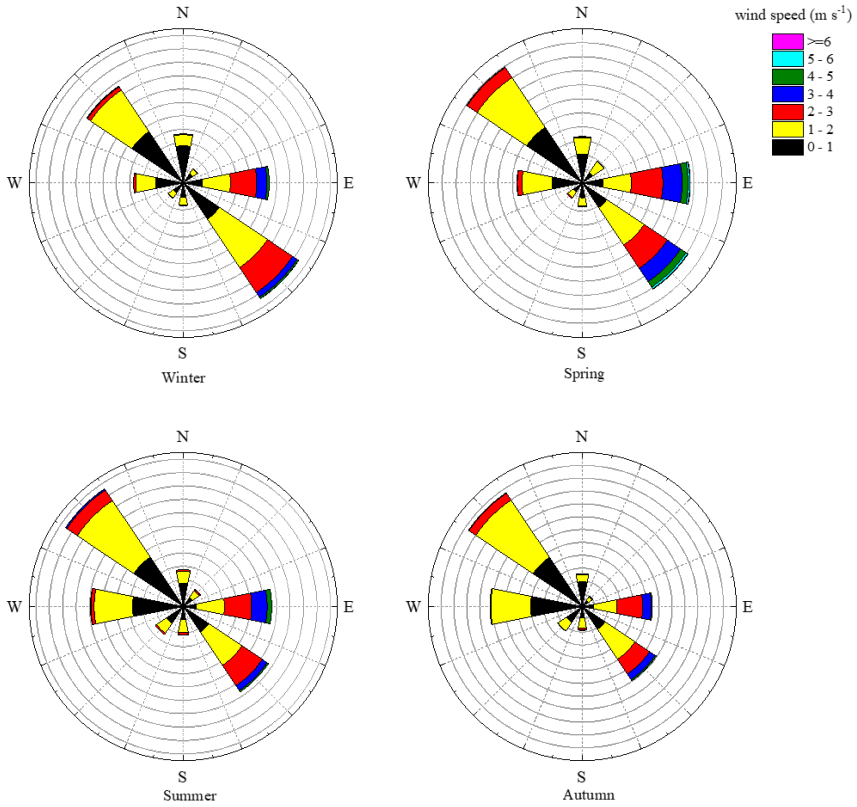

Figure S3. Seasonal wind roses for Baoji.

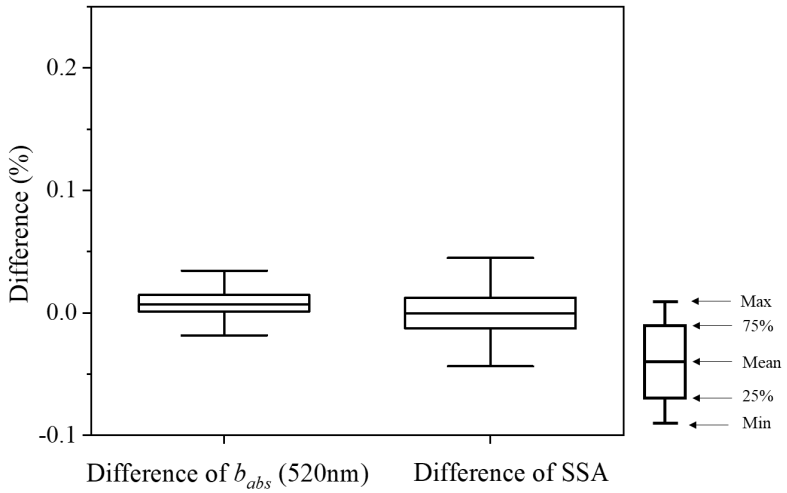

Figure S4. The difference between the modeled b_{abs}(500nm) (respectively, SSA) and the observed b_{abs}(520nm) (respectively, SSA).

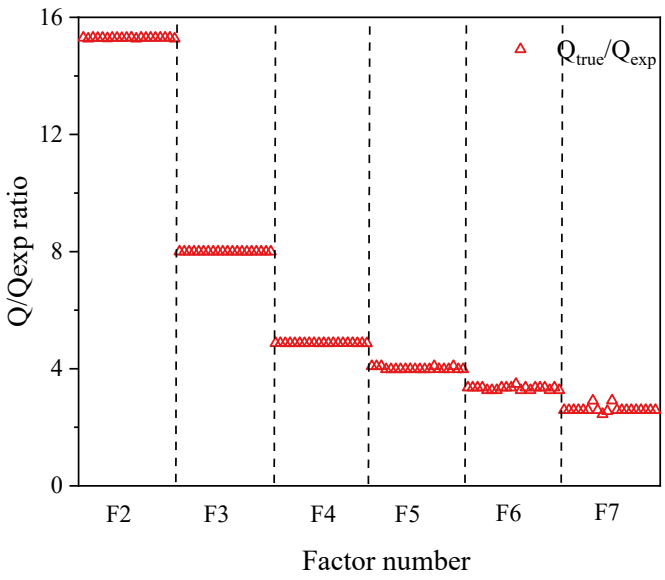

Figure S5. Ratio $Q_{true}/Q_{expected}$ for two to seven factors. The red triangles are the $Q_{true}/Q_{expected}$ values for each run for different factor solutions.

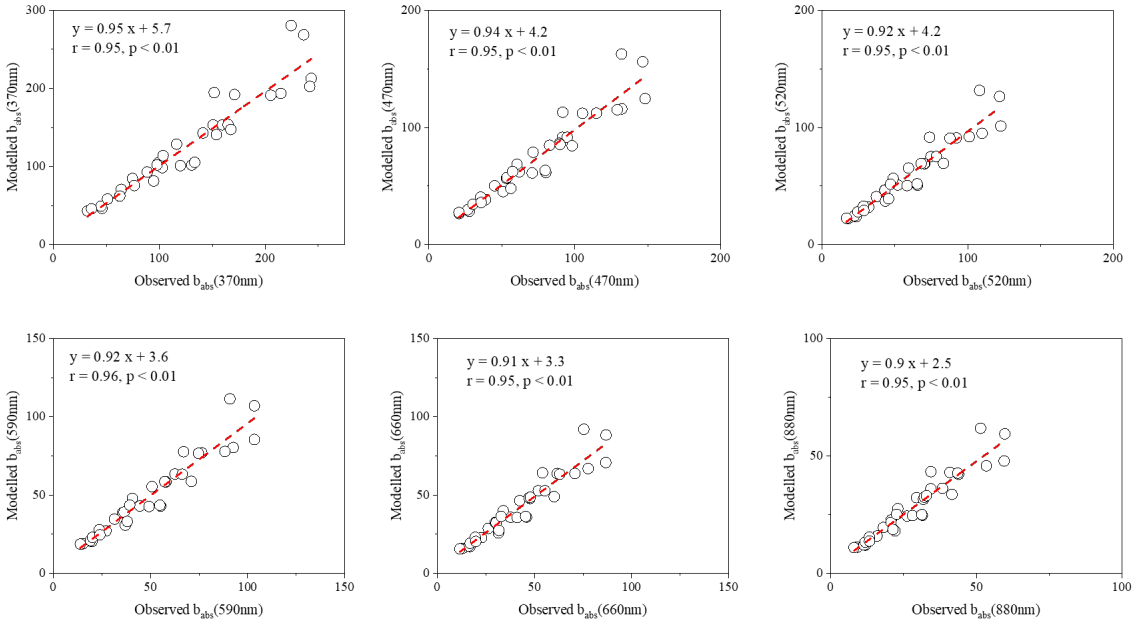

Figure S6. Relationship between the observed daily averaged $b_{abs}(\lambda)$ and positive matrix factorization modeled b_{abs} (λ). λ includes 370, 470, 520, 590, 660 and 880nm. The red line is a linear fit.

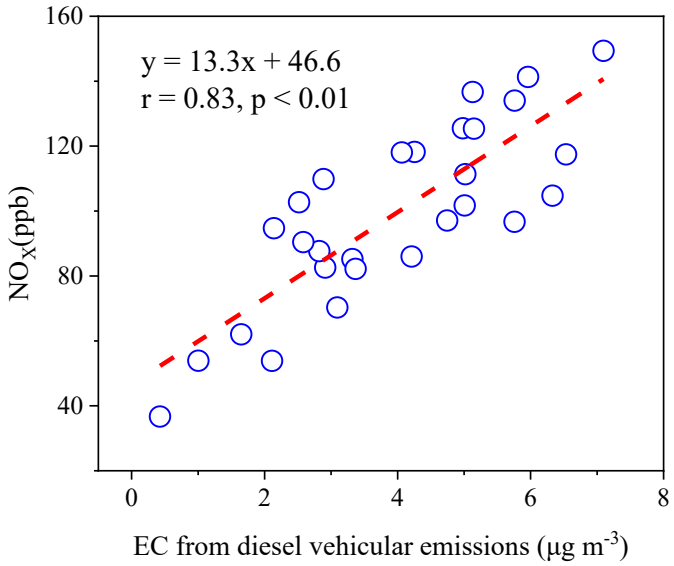

Figure S7. Linear regression of the daily averaged NO_x versus the daily averaged elemental carbon (EC) emitted from diesel vehicular emissions. The red line is the linear fit.

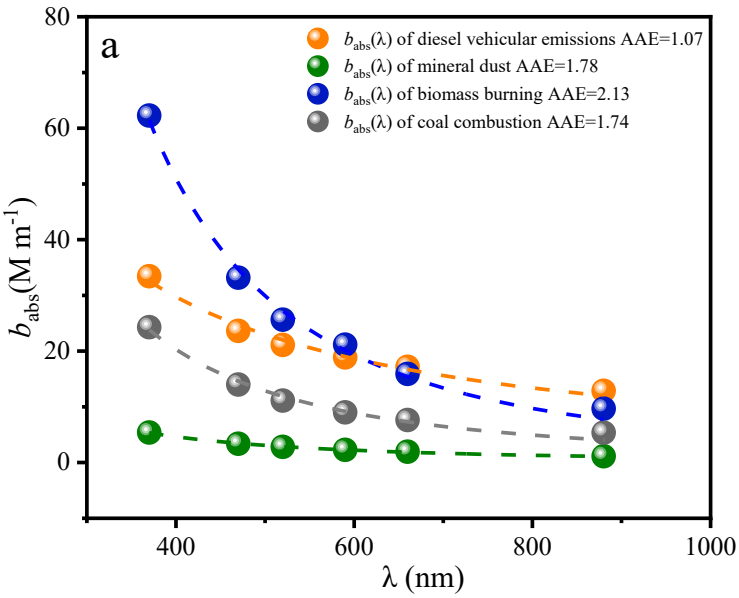

Figure S8. Light absorption ($b_{abs}(\lambda)$) for diesel vehicular emissions, biomass burning, coal combustion, and mineral dust. The dashed lines are the power law fits.

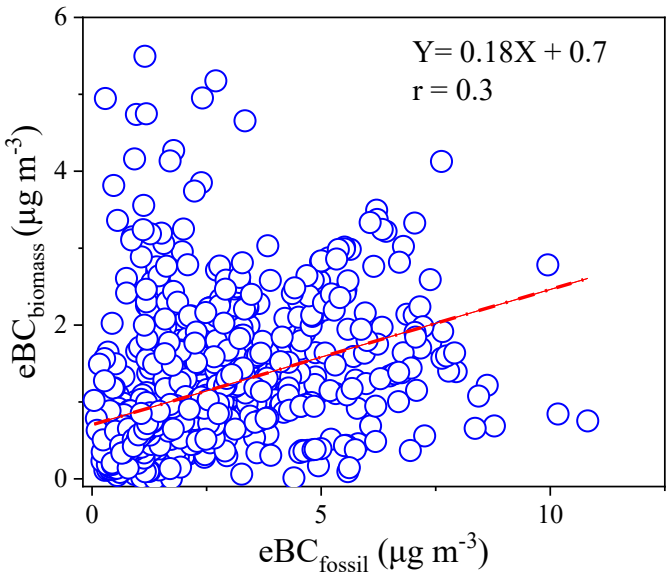

Figure S9. Relationship between hourly averaged eBC from biomass burning ($eBC_{biomass}$) and the eBC emitted from fossil fuel combustion (eBC_{fossil}). The red line is a linear fit.

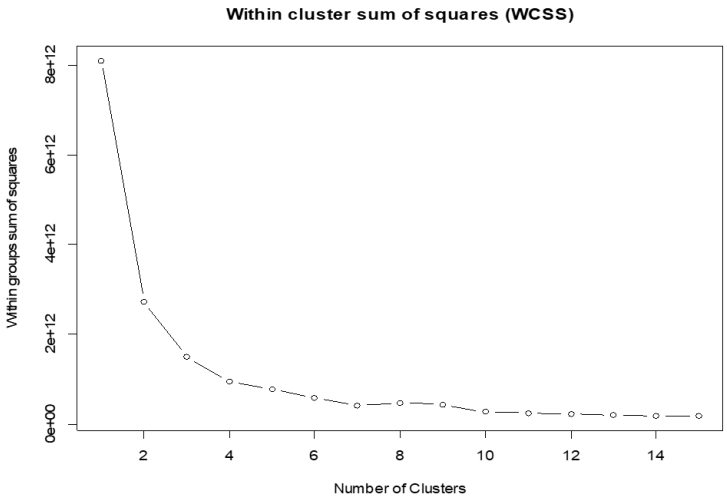

Figure S10. Results of the K-means cluster method

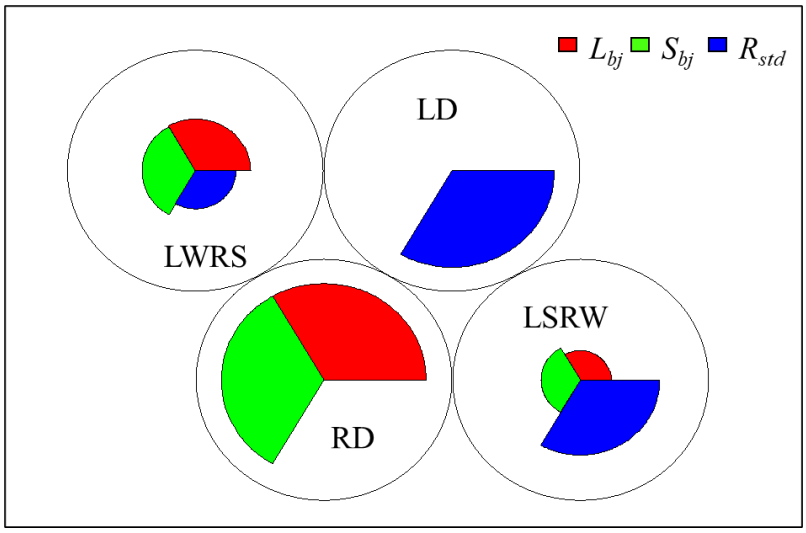

Figure S11. The result of the self-organizing map, sectorial shape represents each variable (L_{bj}, S_{bj} and R_{std}), the bigger the size the larger this variable. The four circles with the sectorial color together indicate the features of the four motion categories. The bottom left circle means high L_{bj} and S_{bj} but low R_{std}, which indicates the feature of regional scale dominance (RD) category. The bottom right represents the high R_{std} but relatively low L_{bj} and S_{bj} indicating local scale strong and regional scale weak (LSRW). The upper left represents local scale weak and regional scale strong (LWRS) and the upper right represent local scale dominance (LD).

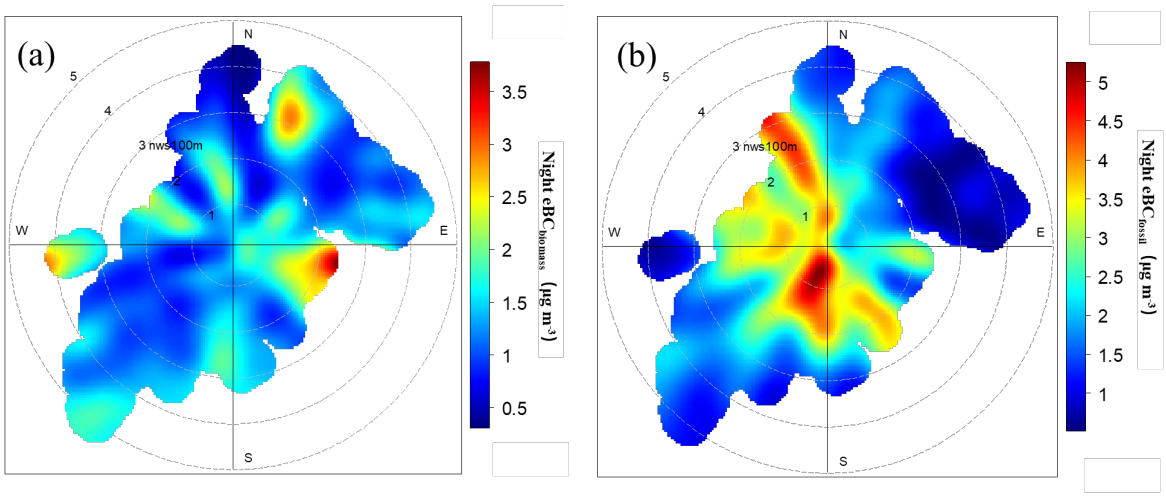

Figure S12. Non-parametric wind regression plots for $eBC_{biomass}$ (a) and eBC_{fossil} (b) at night. The radial and tangential axes represent the wind direction (°) and speed (m s^{-1}), respectively, nws100m represents the night wind speed 100m above the ground level.

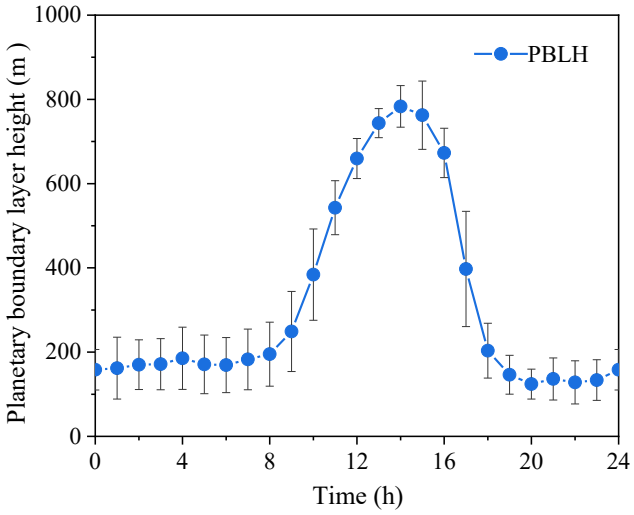

Figure S13. Diel variations of planetary boundary layer height (PBLH, m) under the dominance of regional scale of motion (RD), the blue dots represent the hourly-averaged PBLH and the black lines represent the standard deviations for each point.

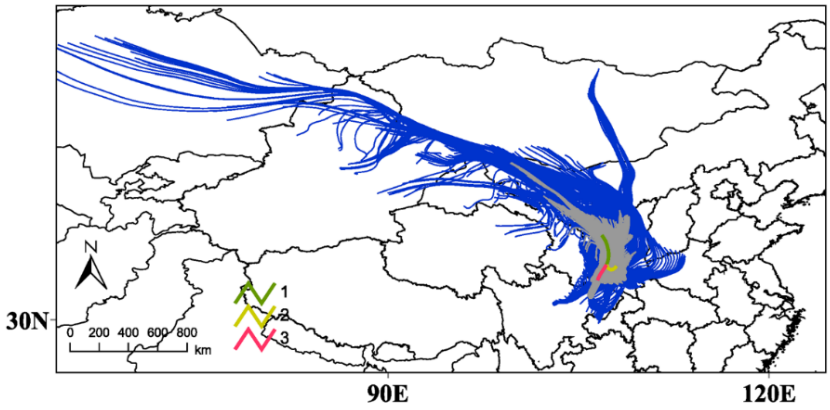

Figure S14. 24h-backward in time air mass trajectories (grey lines) and 72h-back trajectories (blue lines), and trajectory clusters at the sampling site 100 m above the ground. The green line represents Cluster No. 1, the yellow line represents Cluster No. 2, and the red line represents Cluster No. 3.